

# Recognizing Street Lighting Poles From Mobile LiDAR Data

Han Zheng, Ruisheng Wang, and Sheng Xu

**Abstract**—In this paper, a novel segmentation and recognition approach to automatically extract street lighting poles from mobile LiDAR data is proposed. First, points on or around the ground are extracted and removed through a piecewise elevation histogram segmentation method. Then, a new graph-cut-based segmentation method is introduced to extract the street lighting poles from each cluster obtained through a Euclidean distance clustering algorithm. In addition to the spatial information, the street lighting pole’s shape and the point’s intensity information are also considered to formulate the energy function. Finally, a Gaussian-mixture-model-based method is introduced to recognize the street lighting poles from the candidate clusters. The proposed approach is tested on several point clouds collected by different mobile LiDAR systems. Experimental results show that the proposed method is robust to noises and achieves an overall performance of 90% in terms of true positive rate.

**Index Terms**—Gaussian mixture model (GMM), graph cuts, mobile LiDAR, street lighting poles recognition.

## I. INTRODUCTION

**D**ETECTING and recognizing aboveground objects such as street lighting poles, traffic lights, cars, and building facades are important for autonomous driving, detailed 3-D map generation, road infrastructure inventory, and monitoring. Localization of a vehicle’s position is a key problem in autonomous driving field [1], [2]. Knowing the positions of corresponding road infrastructures will be helpful to localize the vehicles, particularly in the area where Global Positioning System signal is too weak to provide navigation information. Another application lies in the area of road infrastructure inventory. Road infrastructure corridors require periodic inspection in order to monitor conditions of lighting poles, signs, and pavements, with a view to improve road safety and economic efficacy by timely maintenance. Currently, this process is expensive and tedious as it requires many “man” hours of traditional surveying or ground-based manual visual inspection. There is a need for system which enables automated inventory and inspection of road infrastructure, and this paper will provide the solution to this gap. Proactive monitoring of civil infrastructure will produce enormous cost savings associated with maintenance and replacement for all levels of government, all over the world. The proposed noncontact imaging method (i.e.,

Manuscript received July 22, 2015; revised February 4, 2016 and June 19, 2016; accepted September 4, 2016.

The authors are with the Department of Geomatics Engineering, Schulich School of Engineering, University of Calgary, AB T2N 1N4, Canada (e-mail: han.zheng@ucalgary.ca; ruiswang@ucalgary.ca; sheng.xu@ucalgary.ca).

Color versions of one or more of the figures in this paper are available online at <http://ieeexplore.ieee.org>.

Digital Object Identifier 10.1109/TGRS.2016.2607521

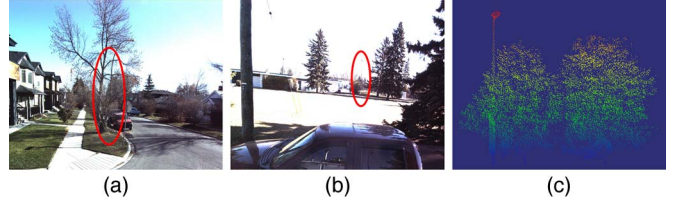


Fig. 1. Examples of challenging situations in images and point clouds. (a) and (b) Occlusion problem and illumination problem in images. (c) Interference problem in point clouds.

LiDAR) will decrease risks associated with the requirement for maintenance crews to be physically out on the road.

Detecting and recognizing polelike objects are always challenging for image-based methods, where illumination changes, occlusions, and various types of the targets will cause problems. Since linear features are the most important characteristics of polelike objects, edge detection methods are used in both [3] and [4] to locate the polelike targets from the images. Nevertheless, these methods work well on simple scenes where polelike objects are isolated from their surroundings and under good illumination conditions. Once occlusions or illumination changes happen, which is quite common in outdoor street scene, as shown in Fig. 1(a) and (b), the image-based methods are found to deteriorate. Different from optical cameras collecting color and brightness information from the scene, laser scanners collect distance information from the surface of each object to the center of the laser scanner. Therefore, when objects are occluded from current view in the 2-D images, they may still be isolated from each other in 3-D point clouds. In addition, shadow and brightness issues in 2-D images no longer exist in 3-D point clouds. In both [3] and [4], forward intersection is used to calculate the position of polelike objects from stereo images, which always involves a feature-matching process, which is time consuming and error prone. However, in LiDAR point clouds, georeferenced 3-D coordinates are known for each point, and the detection is based on 3-D information rather than on color or intensity information, etc.

Mobile LiDAR is a newly emerging technology that can be used in a variety of applications such as 3-D city model generation. Compared with the airborne LiDAR systems, mobile LiDAR systems can collect higher density point clouds and have a detailed view of the objects at ground level. Numerous approaches have been proposed on road extraction [5]–[7], pedestrian detection [8], car detection [9], building facade detection [10]–[13], window detection [14], and road furniture detection (i.e., traffic signs and street lighting poles) [15]–[17]. In general, the point clouds are unorganized,

incomplete, and unevenly distributed. The segmentation is a key step in several applications [18] such as 3-D object recognition and surface reconstruction. Existing methods for segmentation can be classified into four main categories: geometric-primitive-based methods [19], [20], shape-based methods [21], [22], voxel-based methods [23]–[26], and graph-cut-based methods [17], [27]. In geometric-primitive-based methods, abiding by the fact that points from the same object share similar geometric characteristics, geometric primitive cues such as curvature [19] and normal [20] are employed for the segmentation. Shape-based methods rely on the assumption that objects can be modeled by a combination of several basic shapes [22], [28]. These methods are found to have better performance for indoor scenes with little interference than outdoor scenes. In general, voxel-based methods [23]–[26] divide point clouds into voxels first. Local and regional features [23], [24] are then calculated for each voxel, and a multiscale conditional random field method is introduced to classify the voxels. In [25], a link-chain approach is employed to group the voxels into objects and, subsequently, use geometrical models and local descriptors to analyze the objects. Due to the simplified operation in voxel generation, voxel-based methods are usually efficient. However, the segmentation results are always influenced by the fixed size of the voxels. To better deal with the fixed size problem, Yang *et al.* [26] proposed a super-voxel-based hierarchical segmentation method. In [26], ground points are first removed. Then, for nonground point clouds, two different sizes of the super voxels are generated according to the point's color and intensity attributes. According to a set of predefined rules with a hierarchical order, the segment sets obtained through a graph-based segmentation method are classified into different objects.

Graph-cut-based methods [29], [30] are introduced for 3-D point cloud segmentation. In [27], a foreground point is assigned to each object after removing the ground, and a candidate background radius is set as the target segmentation area. Finally, a min-cut-based method is employed to segment the points into foreground and background. In [17], nonground points are grouped into isolated clusters through a Euclidean clustering method. For those clusters in which the surrounding objects such as trees are close to the street lighting poles, a normalized cut method is employed to segment the street lighting poles from the trees.

Once the objects in the point clouds are isolated from each other, it is easier to locate and recognize the objects. Due to the fact that mobile LiDAR systems are relatively new technology [16], only a few approaches have been proposed for polelike object extraction. In [15], cylindrical characteristics of vertical poles are employed to extract vertical polelike objects. In [21], a scan line segmentation approach is employed to extract polelike objects. In [17], a so-called pairwise 3-D shape context method is proposed to semiautomatically extract street lighting poles through the similarity of the shape context between the testing data and the sample data.

In this paper, a novel automatic approach is introduced to extract and recognize the street lighting poles from mobile LiDAR data. Initially, the ground points are removed through a piecewise histogram segmentation method. Then, a Euclidean clustering method is employed to group the nonground points

into clusters. For each cluster containing more than one object, a graph-cut-based method with a novel energy function is formulated to segment the cluster. Finally, street lighting poles are recognized through modeling all the isolated clusters with a Gaussian mixture model (GMM) and matching with the sample street lighting poles' model via the Bhattacharyya distance. The contributions of the proposed approach are twofold.

- 1) In the segmentation step, both the spatial information and the shape information are employed in modeling the data term, and the intensity information is employed in modeling the smoothness term. The existing methods [17], [27] take only the spatial information into consideration and result in a good performance for those spatially separated objects. However, it is not that useful for the clusters where different objects are close to each other, as shown in Fig. 1(c). According to the experimental results, the introduced segmentation method works for all man-made polelike objects on the streets.
- 2) In the recognition step, a GMM-based method is introduced to model the clusters, and a model matching method is employed to evaluate the similarity between the testing data and the training sample. To the best of our knowledge, GMM for street lighting pole recognition has not been considered so far in the literature. The proposed method recognizes the street lighting poles from mobile LiDAR data automatically.

The rest of this paper is organized as follows. The proposed method is presented in Section II. Experimental results are shown and analyzed in Section III. In Section IV, conclusions and future work are discussed.

## II. METHOD

### A. Road Extraction

In [17] and [31], candidate curb points are first located by a profile analysis method. Then, through fitting the ascertained curb points, the boundaries of the road, namely, the curb lines, are generated. Finally, points inside the boundaries are labeled as the road surface. While this method performs well in urban areas, it is found to produce poor results in rural areas. In this paper, a piecewise elevation histogram is introduced to deal with the street scenes in both urban and countryside areas. Raw point clouds are first cut into small pieces along the trajectory of the vehicle based on two considerations: the quantity of the points to be processed each time is reduced, and each small piece of data can be processed with the piecewise elevation histogram method for ground removal. Due to the fluctuations along the road, roads in a large area cannot be treated as a flat plane. However, in a small area, small fluctuations of the roads can result in a sharp peak around the elevation of the road surface when all the points are projected to the  $Z$ -axis (see Fig. 2).

For each small piece of the point cloud, an elevation histogram is generated. Then, for each adjacent bins ( $B_i, B_{i+1}$ ), the threshold value  $R_i$  ( $i = 1, 2, 3, \dots, n$ ) is calculated using

$$R_i = \frac{\text{MAX}(B_i, B_{i+1})}{\text{MIN}(B_i, B_{i+1})}. \quad (1)$$

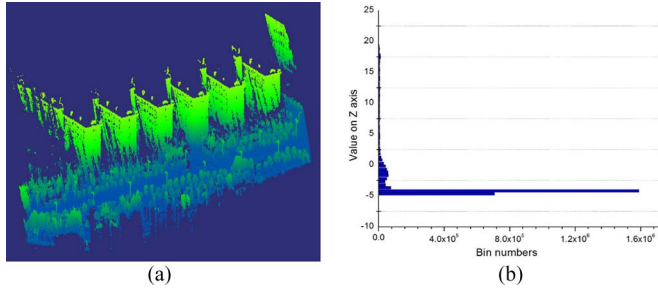


Fig. 2. (a) Small piece of the point clouds. (b) Histogram of the point elevations.

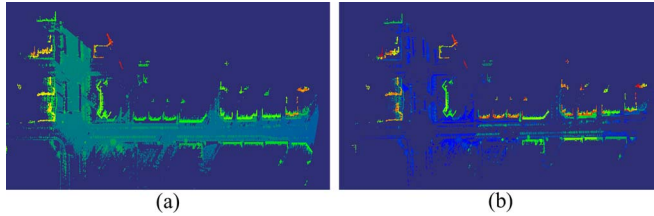


Fig. 3. (a) Point cloud. (b) Nonground point cloud.

The largest value of  $R_t$  ( $1 \leq t \leq n$ ) is obtained first; then, the height value of bin  $t$  is set as the threshold  $Z_g$ . In urban areas, road infrastructures are often built with curbs. In general, the curbs' elevations range from 0.2 to 0.35 m over the road surface. Therefore, to account the curb, the height of the curb  $Z_C$  is added to the value of the segmentation threshold. Then, the raw point cloud  $P$  is segmented into two groups, namely, the ground point cloud and the nonground point cloud, according to

$$\begin{cases} p_i \in G_{\text{ground}}, & p_i^Z \leq Z_g + Z_C \\ p_i \in G_{\text{nonground}}, & p_i^Z > Z_g + Z_C \end{cases} \quad (2)$$

where  $p_i = (p_i^X, p_i^Y, p_i^Z, p_i^I)$  denotes the  $i$ th point ( $1 \leq i \leq n$ ) in the point cloud  $P$ .  $p_i^X$ ,  $p_i^Y$ , and  $p_i^Z$  and  $p_i^I$  denote the point's  $X$ ,  $Y$ , and  $Z$  coordinates and the intensity value, respectively.  $G_{\text{ground}}$  and  $G_{\text{nonground}}$  denote the point clouds of the ground and nonground, respectively. Results are shown in Fig. 3.

### B. Euclidean Distance Clustering

A Euclidean distance clustering method [32] is adopted to group the nonground points into clusters. A KD-tree is first generated to organize the points. Then, points are assigned to a group where the Euclidean distance between each point and its closest point is less than a predefined threshold  $T_d$ . An example of the clustering result is shown in Fig. 4.

### C. Street Lighting Pole Segmentation

As shown in Fig. 4(a), objects separated from each other can be segmented by using the Euclidean distance clustering method. However, in many cases [e.g., Fig. 4(c)], objects close to each other cannot be simply separated by the distance-based clustering method. Furthermore, street lighting pole segmentation always has this problem, and the interference situation is

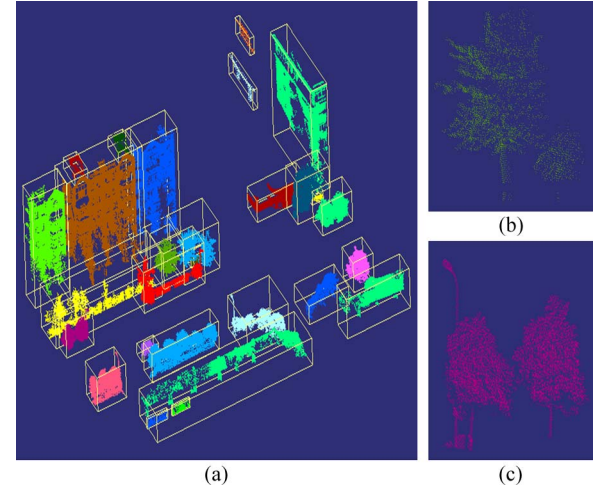


Fig. 4. Results of the nonground point clustering with the Euclidean clustering algorithm. (a) Clustering results. (b) Cluster without interferences. (c) Cluster with interferences.

often discussed as special cases in existing papers [26]. In this paper, we introduce a new graph-cut-based method to address this issue through adding a shape factor to the data term of the energy function and using intensity information for the smoothness term. The proposed segmentation method can be readily applied to segment other polelike objects by tuning the parameters of the shape factor.

**Energy Function Formulation:** Existing graph-cut-based methods can be mainly classified into three categories: min-cut-based method [30], normalized-cut-based method [29], and grab-cut-based method [33]. Different from traditional segmentation algorithms such as region growing [34], watershed segmentation [35], and Canny edge detector [36], all of which use a gradient change for the segmentation, graph-cut-based algorithms employ an energy function which describes the differences between the foreground and the background to achieve the global optima. Building an appropriate energy function which makes best use of the existing information is a key part of the graph-cut-based approaches and can significantly enhance the performance of the method [37].

In object segmentation from point clouds, spatial information is an important factor for separating targets from their surrounding objects. The min cut [27] and the normalized cut [17], which are introduced for segmenting mobile LiDAR data, use only spatial information for the data term. Nevertheless, under some circumstances, particularly when the targets are close to each other, it is difficult to differentiate their surroundings by using only the spatial information [an example is illustrated in Fig. 4(c)].

According to the functionality and manageability of road infrastructures, most of the man-made objects usually conform to a predefined geometrical shape. In general, these objects (particularly for polelike objects) are composed of a few simple geometric shapes such as cylinder and cuboid. This observation results in the proposal of the geometric-primitive-based object extraction methods such as in [19] and [20]. Polelike objects are extracted through detecting the cylindrical features. However,

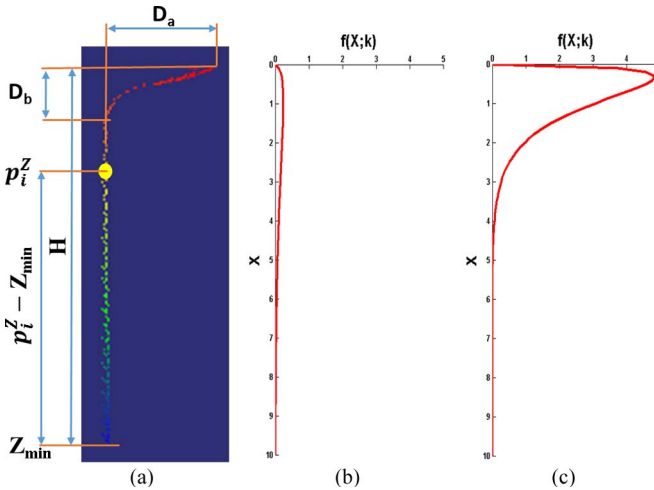


Fig. 5. (a) Most common shape of the street lighting poles. (b) Standard chi-squared probability density function with 3 degrees of freedom. (c) Scaled chi-squared probability density function with 3 degrees of freedom.

these types of methods are very sensitive to interferences (such as a flag hung on a street lighting pole or poles occluded by heavy vegetation). To better address these interference issues, in this paper, we combine the shape information with the spatial information to form the data term in the energy function. Based on the observation that the key components of a street lighting pole are a cylindrical pole and a lamp arm, a chi-square function is introduced to represent the shape, as follows:

$$f(x; k) = \begin{cases} \frac{x^{(\frac{k}{2}-1)} * e^{-\frac{x}{2}}}{\Gamma(\frac{k}{2}) * 2^{\frac{k}{2}}}, & x > 0 \\ 0, & x \leq 0 \end{cases} \quad (3)$$

where  $k$  denotes the degrees of freedom (in our experiments, we set  $k = 3$ ),  $x$  is the value of the variance, and  $\Gamma$  denotes the Gamma function, i.e.,

$$\Gamma(t) = \int_0^\infty x^{t-1} e^{-x} dx. \quad (4)$$

In (4),  $t$  denotes complex numbers with nonpositive integers.

As shown in Fig. 5, the scaled chi-squared probability density function shows a similar shape trend with the street lighting poles along the  $Z$ -axis under the street lighting poles' coordinate system. Thus, we can model the shape of the street lighting poles with the scaled chi-square function as

$$F(x; k) = a * f(b * (H - (p_i^Z - Z_{\min})) ; k) \quad (5)$$

where  $a$  and  $b$  are the scale factors of the probability density function of the chi-squared distribution and the variance of the points along the  $Z$ -axis, respectively.  $H$  is the height of the sample street lighting poles.  $Z_{\min}$  denotes the least  $Z$ -coordinate value of the points in the cluster. The parameters  $(a, b, H)$  are determined by the sample street lighting pole models which are obtained beforehand (sample model training is discussed in Section II-D). More specifically, the scale factor  $a$

is determined by the length of the lamp's arm  $D_a$  [as illustrated in Fig. 5(a)], as follows:

$$a = \frac{D_a}{f_{\max}(x; k)} \quad (6)$$

where  $f_{\max}(x; k)$  denotes the maximum value of the chi-square function with  $k$  degrees of freedom. On the other hand, the scale factor  $b$  is determined by the height of the lamp's arm  $D_b$ , as follows:

$$b = \frac{D_b}{\Delta \text{Dist}} \quad (7)$$

where  $\Delta \text{Dist}$  denotes the difference value between the two variables obtained by solving the equation  $f(x; k) = 0.1$ .

In fact, through a slight modification of the chi-square function with some shift and scaling, the shape of any polelike object can be modeled and, thus, can be extracted with the proposed method.

*Data Term:* Since the shape factor is determined by using the sample models of the street lighting poles, the data term can be written as

$$D_p(f_p) = e^{-\frac{(p_i^{X,Y} - p_C^{X,Y})^2}{(1+F(x;k))^2 * \sigma_{X,Y}^2}} \quad (8)$$

where  $p_i^{X,Y}$  and  $p_C^{X,Y}$  denote the coordinates of the point  $p_i$  and the foreground point  $p_C$  on the  $XY$  plane, respectively.  $\sigma_{X,Y}$  is the standard deviation of the distance between the point  $p_i$  and the foreground point  $p_C$ . In our experiments, the value of  $\sigma_{X,Y}$  is always set to 1.0.

Using the newly introduced shape factor, more accurate segmentation results are obtained, as shown in Fig. 8.

*Smoothness Term:* Instead of repeatedly using the spatial information to model the smoothness term as in [27], in this paper, the intensity information of the point clouds is taken into consideration. Based on the fact that points corresponding to the same material share similar intensities, point clouds can be classified into different groups through material differences. Therefore, a graph is generated by connecting the nearest point pairs through the  $K$ -nearest neighbor method. The function for describing the smoothness term in this paper is

$$V_{pq}(f_p, f_q) = e^{-\frac{(p_i^I - p_j^I)^2}{\sigma_I^2}} \quad (9)$$

where  $p_i^I$  and  $p_j^I$  ( $i \neq j$ ) denote the intensity values of the points  $i$  and  $j$ , respectively.  $\sigma_I$  denotes the standard deviation of the intensity value.

By combining the proposed data term [see (8)] and smoothness term [see (9)], we obtain the new energy function for the graph  $G(V, E)$  of each small cluster, i.e.,

$$E(f) = \sum_{p_i \in V} e^{-\frac{(p_i^{X,Y} - p_C^{X,Y})^2}{(1+F(x;k))^2 * \sigma_{X,Y}^2}} + \lambda \sum_{(i,j) \in V} e^{-\frac{(p_i^I - p_j^I)^2}{\sigma_I^2}} \quad (10)$$

where  $V$  is the vertex set which contains all the points in the small cluster,  $e^{-((p_i^{X,Y} - p_C^{X,Y})^2 / (1+F(x;k))^2 * \sigma_{X,Y}^2)}$  represents the weight of the  $n$ -link edges, and  $e^{-((p_i^I - p_j^I)^2 / \sigma_I^2)}$  captures the

weight of the  $t$ -link edges. The sum of the  $n$ -link and  $t$ -link edges constitutes the edge set  $E$  in the graph.

#### D. GMM-Based Modeling and Recognition

Although the targets can be segmented out from the raw point clouds, a few false alarms having similar shape or features such as traffic signs and power poles can still be present in the segmented results. Existing methods [17], [38] are either sensitive to the noisy points or not affine invariant. In this paper, rather than using local features or geometric primitives to model the targets, we introduce a statistical method which takes the whole object into consideration through modeling the point distributions of the object.

*Local Coordinate System:* The point distributions in the  $XY$  plane and the  $Z$ -axis are used to model the segments obtained by the proposed segmentation approach and then match the segments with the generated sample models. Thus, a unified coordinate system is needed to guarantee the point distributions between two different clusters sharing the same reference frame. Therefore, a local coordinate system is established for each segment.

For each cluster, points are first projected onto the  $XY$  plane, and the two principal components of the point sets are calculated through the principal component analysis (PCA) [39]. The two axes of the local coordinate system  $L$  are parallel to the first and second principal components, respectively. Then, a 2-D grid is generated for the point sets, and the center  $O(p_C^X, p_C^Y)$  of the densest cell is set as the origin of the local coordinate system. Finally, coordinates of the point  $(p_i^x, p_i^y)$  in the local coordinate system  $L$  can be derived from the coordinates  $(p_i^X, p_i^Y)$  in the global coordinate system  $G$  through the following transformation equation:

$$\begin{bmatrix} p_i^x \\ p_i^y \end{bmatrix} = \begin{bmatrix} \cos \theta & -\sin \theta \\ \sin \theta & \cos \theta \end{bmatrix} \begin{bmatrix} p_i^X \\ p_i^Y \end{bmatrix} + \begin{bmatrix} p_C^X \\ p_C^Y \end{bmatrix} \quad (11)$$

where  $\theta$  is the angle between the first principal component of the point sets and the  $X$ -axis of the global coordinate system  $G$ . The relationship between the two coordinate systems is illustrated in Fig. 6, where  $X$  and  $Y$  represent the two axes of the global coordinate system.

*Mixture of Gaussian Modeling:* As shown in Fig. 7, different objects in 3-D space result in different point distributions. For example, for polelike objects, such as street lighting poles, sharp peak can be found on the very top of the street lighting poles in the histogram of the point distribution projected on the  $Z$ -axis [see the third picture in Fig. 7(a)]. However, for the trees, the peak is shown in the middle [see the third picture in Fig. 7(b)].

Based on this fact, we represent each isolated cluster by two point distributions, i.e., the point distributions on the  $XY$  plane and the  $Z$ -axis. In order to better describe the distribution of the points, we introduce the GMM to model the distribution. The equation of the mixture of Gaussian is as follows:

$$g = \sum_{i=1}^K w_i g(X; \mu_i, \Sigma_i) \quad (12)$$

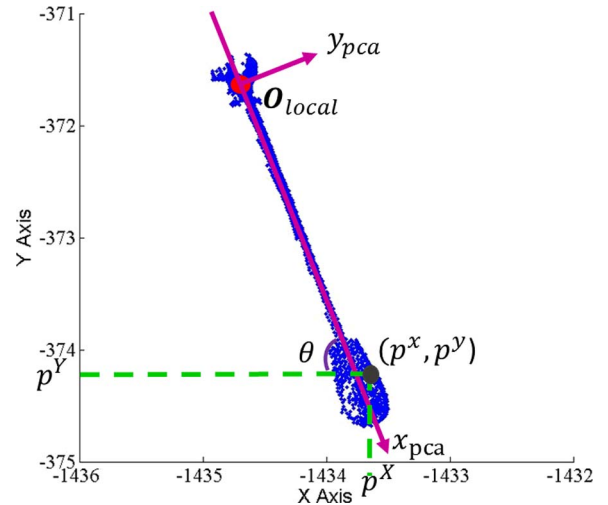


Fig. 6. Transformation between the global and local coordinate systems.

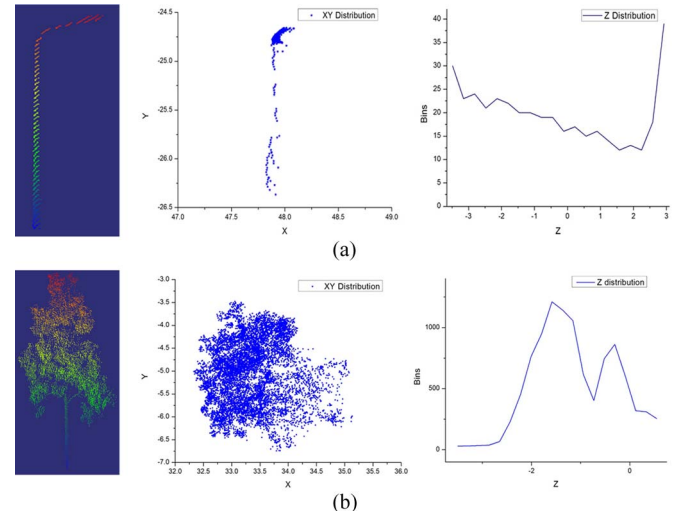


Fig. 7. Street lightning pole's and tree's point distributions on the  $XY$  plane and the  $Z$ -axis. (a) Street lightning pole's distribution on the  $XY$  plane and the  $Z$ -axis. (b) Tree's distribution on the  $XY$  plane and the  $Z$ -axis.

where  $w_i$ ,  $\mu_i$ , and  $\Sigma_i$  represent the weight, mean, and covariance matrix of the  $i$ th Gaussian component of the  $K$  mixtures, respectively.

Then, each of the clusters is defined as  $O \equiv (g_{XY}, g_Z)$ , where  $g_{XY}$  and  $g_Z$  represent the GMMs of the point distribution on the  $XY$  plane and the  $Z$ -axis, respectively.

*Model Selection:* A sample model database is generated at the beginning. The models corresponding to the street lighting poles are manually extracted and saved as samples. Sample models are selected from the candidates subjected to the following rules: 1) each type of the street lighting poles in the point clouds should have one sample; 2) all the samples are fully scanned point cloud, more specifically, without any missing part; and 3) the number of noisy points should be as small as possible.

*Model Matching:* To measure the similarity between the two distributions, we introduce the Bhattacharyya distance [45]. Derived from the Bhattacharyya coefficient, the Bhattacharyya

TABLE I  
DESCRIPTION OF THE DATA SETS AND THE GROUND TRUTH OF THE STREET LIGHTING POLES IN THE DATA SETS

Dataset	Scanner	Datasets Description			Ground Truth street lighting Poles		
		Point Density (points/m <sup>2</sup> )	Total Points	Type	Without Interferences	With Interferences	Total
I	Optech Lynx MGI	679.5	34,219,070	Urban	40	53	93
II	Optech Lynx MGI	1019.2	20,072,546	Suburb	21	2	23
III	Optech Lynx SGI	3784.6	203,194,264	Urban	75	20	95
IV	VIEGL VMX-450	3554.1	342,647,811	Suburb	21	9	30

distance is proposed to evaluate the similarity between two probability distributions. For two probability distributions  $P$  and  $Q$  which share the same domain  $X$ , the Bhattacharyya coefficient  $C_B$  is defined as

$$C_B = \int \sqrt{P(x)Q(x)}dx. \quad (13)$$

The Bhattacharyya distance  $D_B$  is defined as

$$D_B = -\ln(C_B). \quad (14)$$

The range of the Bhattacharyya distance is from 0 to positive infinity. The closer the two probability distributions are, the more likely the distance is close to zero. In this paper, the two probability distributions are Gaussian functions; it can be readily derived from the Bhattacharyya distance  $Bha(g_i, g_j)$  via substituting the Gaussian functions into (13) and (14) as [41]

$$\begin{aligned} Bha(g_i, g_j) &= \frac{1}{8}(\mu_i - \mu_j)^T \left( \frac{\Sigma_i + \Sigma_j}{2} \right)^{-1} (\mu_i - \mu_j) \\ &\quad + \frac{1}{2} \ln \frac{\left| \frac{\Sigma_i + \Sigma_j}{2} \right|}{\sqrt{|\Sigma_i||\Sigma_j|}} \end{aligned} \quad (15)$$

where  $g_i$  and  $g_j$  are the two Gaussian distributions; and  $\mu_i$ ,  $\Sigma_i$  and  $\mu_j$ ,  $\Sigma_j$  represent the mean and covariance matrices of  $g_i$  and  $g_j$ , respectively.

Since the models of both the objects and the samples in the database are GMMs, the definition of the similarity between the two GMMs can be given by [40]

$$D(g^S, g^T) = \sum_{i=1}^K \sum_{j=1}^K w_i w_j Bha(g_i^S, g_j^T) \quad (16)$$

where  $g^S$  and  $g^T$  are Gaussian models with  $K$  mixtures;  $g_i^S$  and  $g_j^T$  are the corresponding kernel parameters of  $g^S$  and  $g^T$ , respectively; and  $w_i$  and  $w_j$  are the weights of the  $i$ th and  $j$ th mixtures of the Gaussian model of  $g^S$  and  $g^T$ , respectively.

Finally, those clusters with Bhattacharyya-based distances ( $D_{XY}, D_Z$ ) that are smaller than the predefined distance threshold  $D(T_{XY}, T_Z)$  [see (17)] are labeled as the street lighting poles  $\mathcal{L}$ , i.e.,

$$\mathcal{L} = \begin{cases} 1, & D_{XY} \leq T_{XY} \cap D_Z \leq T_Z \\ 0, & \text{otherwise.} \end{cases} \quad (17)$$

### III. EXPERIMENTS AND ANALYSIS

#### A. Data Sets Description

Four data sets collected from three different mobile LiDAR systems containing both urban and suburban areas are tested in this paper. Details of the data sets are presented in Table I. The ground truth of the street lighting poles is generated through manual count in each data set.

#### B. Graph-Cut-Based Segmentation

**Foreground Point Choosing:** As mentioned in Section II-C, the regional penalty is assigned to each point by calculating the similarity between the point and the foreground. In this paper, the spatial information is employed to describe the similarity. Polelike objects always result in a high-density spot at the center position of the pole's base when all the points are projected onto the  $XY$  plane. Therefore, after the Euclidean distance clustering step, points in each cluster containing more than one object are projected to the  $XY$  plane, and spot  $p(X, Y)$  with the highest density is found. Then, the point  $p_C(X, Y, 0)$  is set as the foreground point of the cluster. The closer the points in the cluster to  $p_C$  on the  $XY$  plane are, the smaller the penalty, and the greater the weight is.

**Shape Factor:** Since the penalty of the data term is calculated through the distance between points in the cluster and the foreground point on the  $XY$  plane, a cylinder-shaped boundary will be formed, and those points inside the boundary constitute the foreground object. This method performs well on cylindrical objects such as mail barrels or objects that are separated from each other. However, it fails to separate objects, such as street lighting poles and trees, which are close to each other.

As discussed in Section II-C, the shape information described by a modified chi-squared function is employed in the data term. The comparison of the graph-cut-based segmentation with or without using the shape information is illustrated in Fig. 8.

In Fig. 8, five segmentation examples with the graph-cut-based method are shown. The results of using both the spatial information and the shape information are illustrated in the first row. Results using only the spatial information are shown in the following four rows by an increasing order of the distance deviation value on the  $XY$  plane. It can be observed from Fig. 8(b)–(d) that, as the distance deviation  $\sigma_{X,Y}$  increases, more points belonging to the target (street lighting poles in this paper) are labeled as the foreground. However, along with this, the number of the false-labeled background points

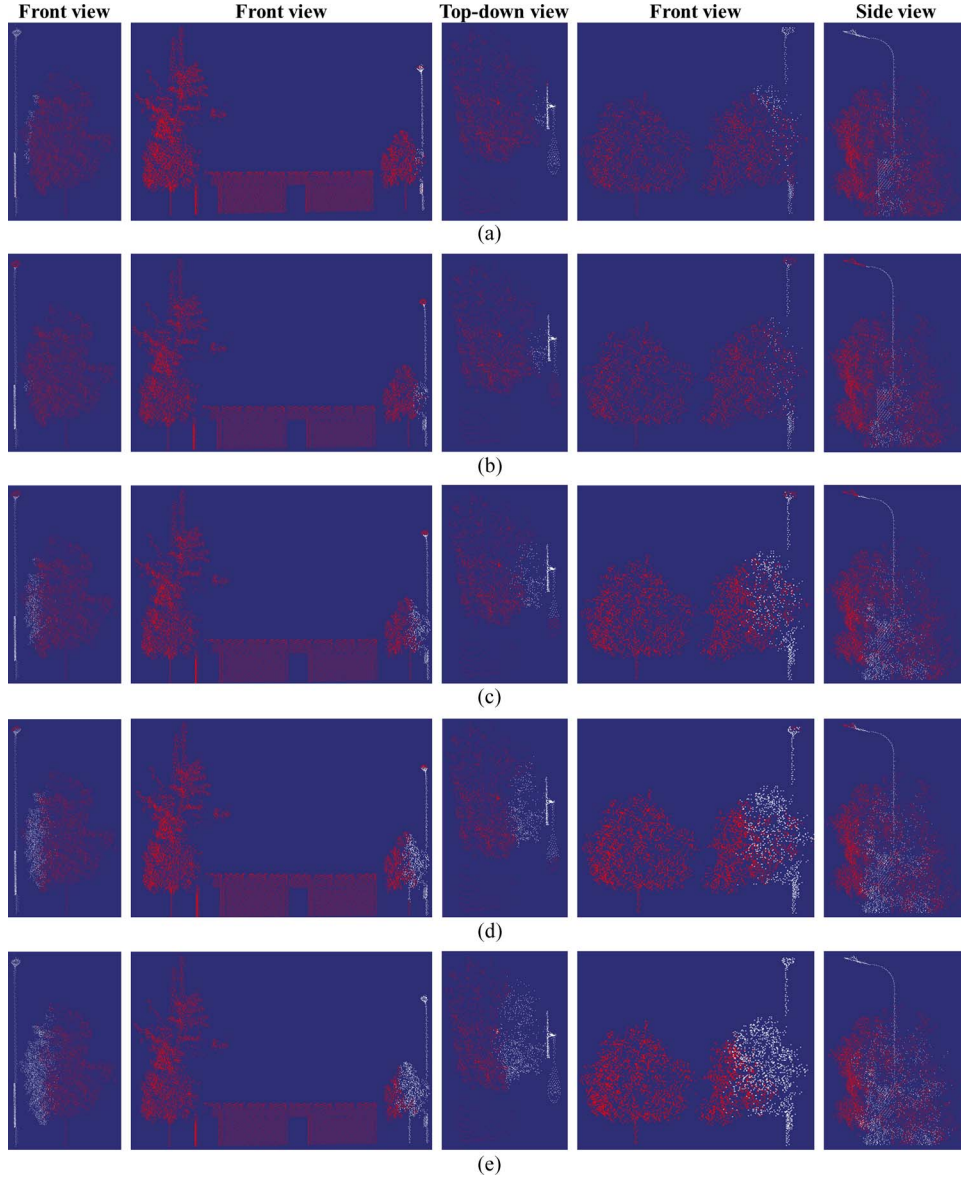


Fig. 8. Examples of graph-cut-based segmentation with or without shape information. The foreground and background points are colored with white and red, respectively. The weights in the smoothness term for all experiments are all equal to 1. (a) Results of using both the spatial information and the shape information in the data term. (b) Results of using only the spatial information on the  $XY$  plane with  $\sigma_{X,Y} = 0.6$ . (c) Results of using only the spatial information on the  $XY$  plane with  $\sigma_{X,Y} = 1.0$ . (d) Results of using only the spatial information on the  $XY$  plane with  $\sigma_{X,Y} = 1.2$ . (e) Results of using only the spatial information on the  $XY$  plane with  $\sigma_{X,Y} = 1.5$ .

TABLE II  
PARAMETERS USED IN THIS PAPER

Datasets	Parameters				
	$\sigma_{X,Y}(m)$	$\sigma_I$	$K$	$T_{XY}$	$T_Z$
I					0.6    0.15
II					1.5    0.15
III	1.0	0.8	2		1.5    0.15
IV					1.5    0.3

also increases. Since the shape information is considered [see Fig. 8(a)], our method achieves the desired performance.

Table II lists the parameters used in the data term. Some of the parameters such as the scale factors  $a$  and  $b$ , the degrees of freedom  $k$  used for the data term, and the predefined height of the street lighting poles  $H$  are calculated from the sample

models. The distance standard deviation  $\sigma_{X,Y}$  controls the radius range of the generated cylinder for the base poles. The larger the value, the bigger the cylinder that will be obtained, and the more noisy points that will be included. The intensity standard deviation  $\sigma_I$  affects the similarity evaluation of the two closest point pairs in the smoothness term. The larger the value, the more likely the noisy points are included. The only parameters that need tuning are the distance thresholds of the matching results. Range thresholds for different data sets are caused by the varied shapes of the street lighting poles and the fixed number of the mixture of Gaussians employed in this paper. Street lighting poles with more complex shapes may not be accurately described with two mixtures. However, with a fixed number of the mixtures, the algorithm performs well on the majority types of the street lighting poles.

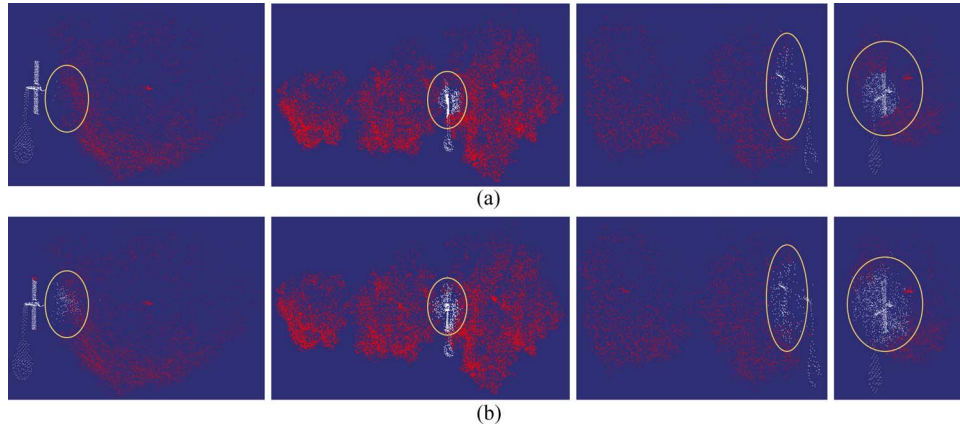


Fig. 9. Results of the graph-cut-based segmentation using either the intensity information or the Euclidean distance in the smoothness term. (a) With intensity information. (b) With distance information.

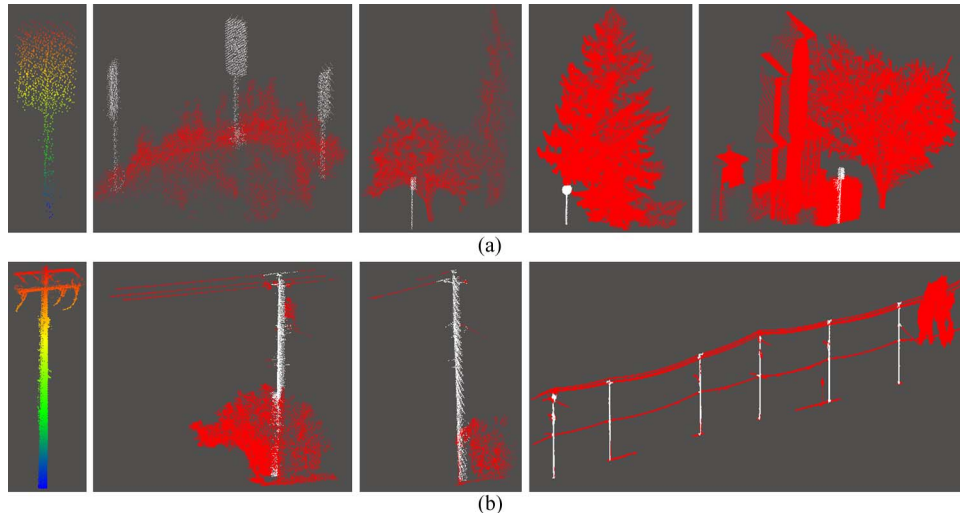


Fig. 10. Segmentation results of other polelike objects with the proposed method. (a) Road sign. (b) Power pole.

**Effect of the Intensity Information:** The smoothness term in a graph-cut-based method measures the nonpiecewise smooth extent. Based on the assumption that neighboring points are more likely to be assigned to the same segment, [27] make use of the Euclidean distance between the point and its closest point for the smoothness term. It works well on separated objects, but it does not work when objects are close to each other. In Fig. 9, the performances of using either the Euclidean distance or the intensity information in the smoothness term are shown.

As indicated in Fig. 9, better performance can be seen in the foreground segment with the proposed method using the intensity information rather than the Euclidean distance for the smoothness term.

**Other Polelike Object Segmentation Experiment:** We tested some other polelike objects such as road signs and power poles, which are occluded by their surroundings. According to the sample models (see the images shown in the first column in Fig. 10), the heights of the road sign and the power pole are 2.3 and 10.5 m respectively. The three parameters ( $a, b, k$ ) of the shape factor calculated through functions 6 and 7 are (0.25, 4, 4) and (0.53, 5, 6). Experimental results shown in Fig. 10 demonstrate that the proposed segmentation method can be

applied to other polelike object segmentation, and road signs and power poles are well segmented.

### C. Street Lighting Poles Recognition With GMM

**Mixture of Gaussian Models:** A mixture of Gaussian modeling method is introduced to model the aboveground objects. For each cluster, the point distributions on both the  $XY$  plane and the  $Z$ -axis are modeled by the GMM ( $g_{XY}$  and  $g_Z$ ), respectively. The plots of the probability density function on the  $XY$  plane ( $\text{PDF}_{XY}$ ) and the  $Z$ -axis ( $\text{PDF}_Z$ ) for six different categories of aboveground objects are illustrated in Fig. 11.

As shown in Fig. 11, different objects have different point distributions on the  $XY$  plane and the  $Z$ -axis. Although trees [see Fig. 11(f)] may have similar point distributions with some of the street lighting poles [see Fig. 11(a)] on the  $Z$ -axis, large differences can be found in their point distributions on the  $XY$  plane. Thus, we can differentiate the street lighting poles from trees through matching the models between the sample street lighting poles and the candidate objects.

**Model Matching:** Based on the differences of the point distributions between various objects, sample models are first

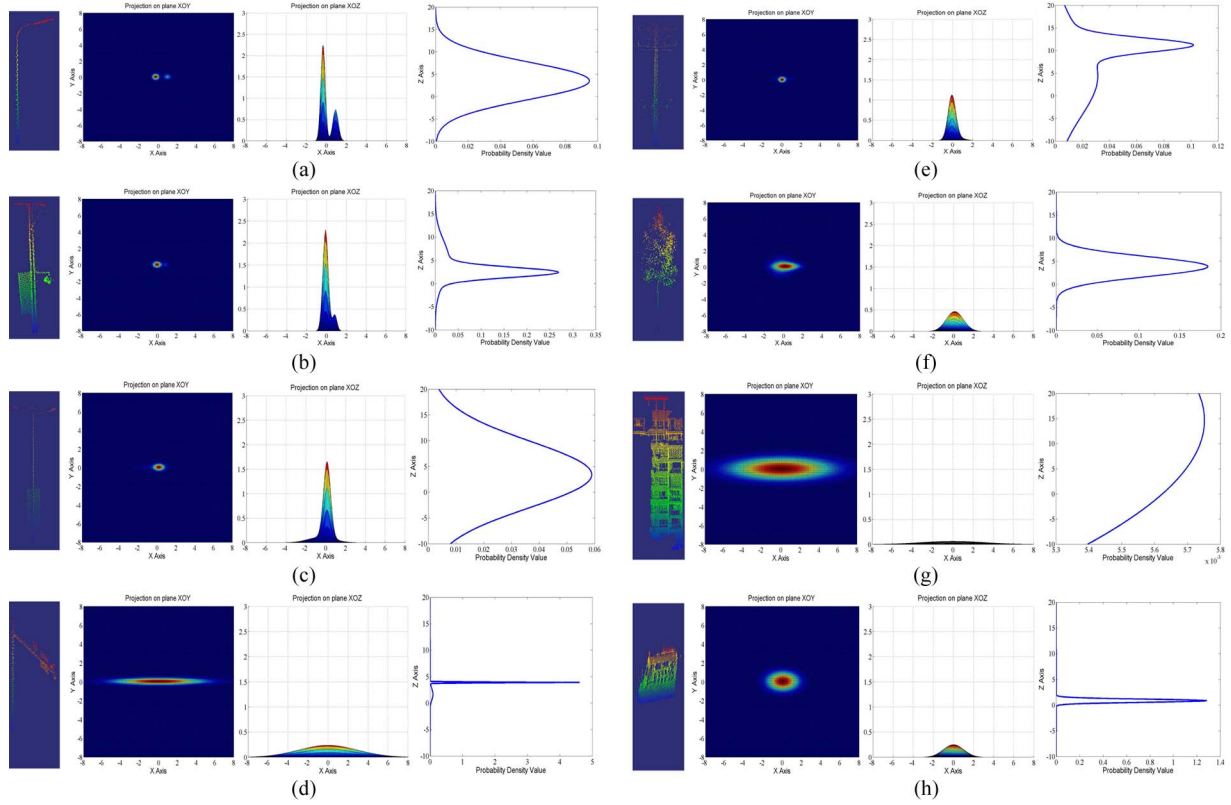


Fig. 11. Aboveground object's modeling results with GMM (in each group, the four figures are ordered by the raw point cloud, the projection of  $\text{PDF}_{XY}$  on the  $XY$  plane, the projection of  $\text{PDF}_{XY}$  on the  $XZ$  plane, and the  $\text{PDF}_Z$  on the  $Z$ -axis). (a) Street lighting pole (Type 1). (b) Street lighting pole (Type 2). (c) Street lighting pole (Type 3). (d) Traffic Sign. (e) Power pole. (f) Tree. (g) Building facade. (h) Car.

TABLE III  
MODEL MATCHING RESULTS

Testing Models	Sample Models								Matched /Total
	D <sub>XY</sub>	D <sub>Z</sub>							
Advertising board	<b>T01</b>	1.009	6.703	0.803	2.068	0.961	0.481	0.967	1.051
	<b>T02</b>	4.014	6.672	2.101	1.665	3.463	0.342	3.615	0.908
Traffic Lights	<b>T03</b>	11.035	0.623	5.755	0.769	9.511	2.856	9.947	0.470
	<b>T04</b>	8.377	2.001	4.381	0.892	7.233	<b>0.086</b>	7.558	0.281
Car	<b>T05</b>	<b>0.552</b>	20.918	<b>0.373</b>	3.598	<b>0.470</b>	0.884	<b>0.451</b>	1.494
	<b>T06</b>	<b>0.577</b>	4.149	<b>0.413</b>	1.132	<b>0.509</b>	0.229	<b>0.498</b>	0.798
Building Facade	<b>T07</b>	1.052	0.738	0.819	0.585	1.003	0.929	1.013	0.508
	<b>T08</b>	1.036	1.887	0.887	0.390	0.997	0.758	1.004	0.344
Power Pole	<b>T09</b>	<b>0.562</b>	0.653	<b>0.102</b>	0.222	<b>0.333</b>	0.703	<b>0.213</b>	0.196
	<b>T10</b>	<b>0.467</b>	0.460	<b>0.116</b>	0.158	<b>0.290</b>	0.557	<b>0.213</b>	0.146
Road Sign	<b>T11</b>	0.676	6.616	<b>0.095</b>	1.579	<b>0.378</b>	0.223	<b>0.222</b>	0.625
Trees	<b>T12</b>	0.657	0.689	<b>0.415</b>	0.830	<b>0.559</b>	1.029	<b>0.536</b>	0.383
	<b>T13</b>	0.789	1.948	<b>0.351</b>	1.133	<b>0.599</b>	0.223	<b>0.536</b>	0.508
	<b>T14</b>	<b>0.367</b>	<b>0.085</b>	<b>0.143</b>	0.191	<b>0.256</b>	0.258	<b>0.219</b>	<b>0.045</b>
	<b>T15</b>	<b>0.363</b>	0.812	<b>0.096</b>	0.578	<b>0.227</b>	0.131	<b>0.176</b>	0.189
Testing Street Lighting Poles	<b>T16</b>	0.925	<b>0.001</b>	<b>0.245</b>	<b>0.061</b>	0.612	0.164	<b>0.472</b>	<b>0.016</b>
	<b>T17</b>	<b>0.377</b>	<b>0.088</b>	<b>0.076</b>	<b>0.066</b>	<b>0.223</b>	<b>0.051</b>	<b>0.154</b>	0.116
	<b>T18</b>	<b>0.327</b>	0.182	<b>0.066</b>	<b>0.015</b>	<b>0.195</b>	0.257	<b>0.141</b>	<b>0.005</b>
	<b>T19</b>	0.883	<b>0.106</b>	<b>0.240</b>	<b>0.143</b>	<b>0.577</b>	<b>0.019</b>	<b>0.476</b>	0.165
	<b>T20</b>	3.741	<b>0.023</b>	2.774	<b>0.011</b>	3.445	0.219	3.597	<b>0.016</b>
	<b>T21</b>	0.768	<b>0.050</b>	0.752	<b>0.049</b>	<b>0.527</b>	<b>0.091</b>	<b>0.569</b>	<b>0.066</b>
	<b>T22</b>	1.821	0.629	1.445	0.666	1.612	<b>0.108</b>	1.710	0.291
	<b>T23</b>	0.601	0.232	<b>0.553</b>	0.302	<b>0.419</b>	<b>0.015</b>	<b>0.462</b>	0.216

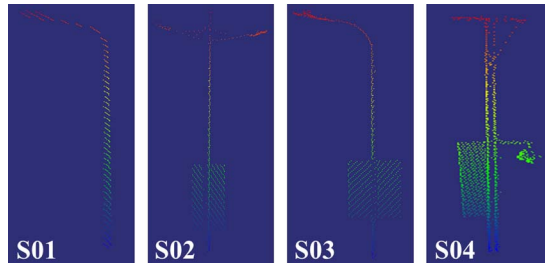


Fig. 12. Sample street lighting poles.

generated for each type of the street lighting poles. Then, for each testing cluster, mixture of Gaussian models on both the  $XY$  plane and the  $Z$ -axis are generated. Finally, the model distance between the testing objects and the training samples is evaluated through the Bhattacharyya-based distance. The matched ones are labeled as the street lighting poles, and the best matched label of the samples is assigned to the corresponding object.

In order to better demonstrate the accuracy of matching, a few other objects were chosen to match with the sample street lighting poles, and the resultant Bhattacharyya distances are listed in Table III. Sample street lighting poles used in this test are shown in Fig. 12, and the testing objects are illustrated in Fig. 13. In Table III, the distances meeting the thresholds (see Table II) are shown in boldface.

As we can see in Table III, objects with different shapes [such as advertising board (T01, T02), building facade (T07, T08), and traffic light (T03, T04)] show large matching distances to the sample models. Although the cars (T05, T06) show similar matching distances as poles on the  $XY$  plane due to incomplete data, large distances can still be found on the  $Z$ -axis. For those polelike objects such as power pole (T09, T10), road sign (T11), and trees (T12-T15), similar point distributions on the  $XY$  plane can be readily found. However, these man-made polelike objects have different heights; for example, road signs and traffic lights are usually shorter than street lighting poles, whereas power poles are higher than all the other man-made objects. Thus, they result in large distances with respect to the  $Z$ -axis from the model matching. For most of the trees, large matching distances can be found between the training samples and the testing objects with respect to the  $Z$ -axis. However, matched false alarms (T14) still exist. Thus, other information such as the density of the pole center can be used to further distinguish the street lighting poles and the false alarms. For the testing street lighting poles (T16-T19), short distances can easily be found on both the  $XY$  plane and the  $Z$ -axis between the training samples and the testing objects. In some cases (T17), one testing street lighting pole is matched with several samples due to their similarities. The testing objects will be labeled by the best matched scores (the smallest square root of the matched distance on both the  $XY$  plane and the  $Z$ -axis). For matching results of the clusters with (T21 and T23) and without (T20 and T22) our method, although distances (T20) with respect to the  $Z$ -axis can be matched, distances on the  $XY$  plane will not be matched for all those unsegmented clusters. Our segmentation method successfully separates the

street lighting poles from the trees and matches with the training samples.

#### D. Statistical Results

In each data set, all the clusters from segmentation are categorized into two classes, namely, the positive class  $P$ , in which the clusters are street lighting poles, and the negative class  $N$ , in which the clusters are nonstreet lighting poles. For each testing cluster  $C$ , a label will be assigned after the model matching process, and a hypothesized positive class  $P_h$  will be generated. Four types of results are obtained: true positive (TP), if  $C \in P \cap P_h$ ; true negative (TN), if  $C \in \bar{P} \cap \bar{P}_h$ ; false positive (FP), if  $C \in P \cap \bar{P}_h$ ; and false negative (FN), if  $C \in \bar{P} \cap P_h$ . Based on these four categories of label results, we can evaluate the accuracy of the recognition results comprehensively through five quantitative indicators [42], namely, true positive rate ( $TPR = TP/(TP + FN)$ ), which describes the probability of true street lighting poles to be recognized, true negative rate ( $TNR = TN/(FP + TN)$ ), which describes the probability of nonstreet lighting poles that failed to be matched with the sample street lighting pole models, positive predictive value ( $PPV = TP/(TP + FP)$ ), which reflects the probability of the true street lighting poles recognized in all the matched results, negative predictive value ( $NPV = TN/(TN + FN)$ ), which describes the percentage of the true nonstreet lighting poles' clusters in all the unmatched clusters, and accuracy ( $ACC = (TP + TN)/(TP + FN + FP + TN)$ ), which shows the overall performance of the recognition results on both TPs and TNs. All the recognition results and evaluation results are listed in Table IV.

In Table IV, for each data set, with only one set of the parameters (as shown in Table II), the TPR of the proposed method reached around 90%. The overall performance of the proposed approach in each data set is shown in Fig. 14. Due to the memory capacity limits of the computer for the visualization of the large data sets, only parts of the results are displayed for data sets III and IV. The detected street lighting poles, false alarms, and ground are colored in red, green, and gray, respectively (see Fig. 14). According to the statistical results, false alarms are mainly small building fragments showing similar shapes as street lighting poles [such as the ones in the right side in Fig. 14(a)], trees [see the left side in Fig. 14(a)], and short power poles [such as in Fig. 14(c)].

#### E. Comparative Studies

**Graph-Cut-Based Segmentation:** In order to better illustrate the performance of the proposed segmentation method, we compared our approach with two existing graph-cut-based methods, namely, the min-cut-based segmentation method [27] and the normalized-cut-based segmentation method [17].

In Fig. 15, six samples were chosen from different data sets, in which samples 1–4 are from data set I (point density: 679.5 points/m<sup>2</sup>) and samples 5 and 6 are from data set IV (point density: 3554.1 points/m<sup>2</sup>) for the performance comparison between three graph-cut-based segmentation algorithms. As shown in Fig. 15, the normalized-cut-based segmentation

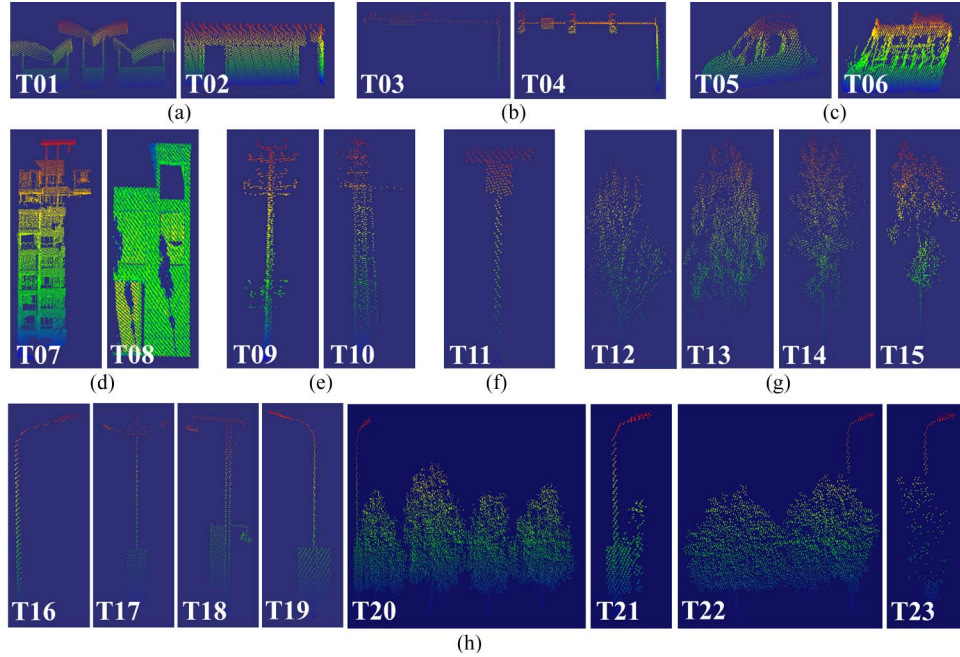


Fig. 13. Testing examples of different aboveground objects. (a) Advertising board. (b) Traffic lights. (c) Car. (d) Building facade. (e) Power pole. (f) Road sign. (g) Tree. (h) Testing lamp poles.

TABLE IV  
STATISTICAL RESULTS AND EVALUATION RESULTS OF THE FOUR DATA SETS

Dataset Number	Recognition Results				Evaluation Results					
	Without Interferences	With Interferences	TP	FP	Total Testing Clusters	TPR (%)	TNR (%)	PPV (%)	NPV (%)	ACC (%)
I	45	38	83	8	2026	89.25	99.59	91.21	99.48	99.11
II	20	2	22	0	1085	95.65	100	100	99.91	99.91
III	72	17	89	15	4080	93.68	99.62	85.58	99.85	99.49
IV	21	7	28	1	4114	93.33	99.98	96.55	99.95	99.93

method achieved acceptable results only if the foreground and the background have a similar number of points, as shown in 3–6 in Fig. 15(b). The min-cut-based segmentation method shows a better performance than the normalized-cut-based method; however, with one set of parameters, oversegmentation [see 3 and 4 in Fig. 15(c)] and undersegmentation [see 5 and 6 in Fig. 15(c)] results can be always obtained. However, with one set of parameters, the proposed segmentation method shows better performance [see Fig. 15(d)].

**Street Lighting Pole Extraction and Recognition:** Here, we evaluate the performance of the proposed algorithm through comparing with other existing methods, including the PCA-based method [43], the Density of Projected Points (DoPP) algorithm [44], and the percentile-based method [16]. Since the algorithm proposed in [44] can be greatly influenced by the tall buildings on both sides of the road, in order to compare these algorithms under the same condition, a preprocessing step is adopted to filter out the points beyond the street lighting poles on both sides of the road. The testing point cloud after preprocessing is shown in Fig. 16(a). A qualitative comparison of the results generated by various algorithms is shown in Fig. 16(b)–(e). As shown in Fig. 16, although many linear feature points on the street lighting poles are detected, the PCA-

based method [see Fig. 16(d)] is the most sensitive one to the interferences of the trees and other objects such as advertisement boards. The percentile-based method [see Fig. 16(c)] and the DoPP algorithm [see Fig. 16(e)] show good performances in terms of the correctness, but the completeness and the conciseness can be easily influenced by the tall trees and the interferences. On the contrary, the proposed method [see Fig. 16(b)] shows good performance in terms of correctness, completeness, and conciseness.

#### IV. CONCLUSION

In this paper, we have proposed an approach for automatic recognition of street lighting poles from mobile LiDAR data. The raw point clouds are first segmented into ground and non-ground objects. Then, a Euclidean distance clustering method is employed to group the nonground point clouds into a series of small clusters. In addition to the spatial information, the shape information and the intensity information are also considered in the graph-cut-based segmentation for each cluster containing more than one object. Finally, a GMM-based method is introduced to model the clusters, and the street lighting poles are recognized through matching the models in the testing data

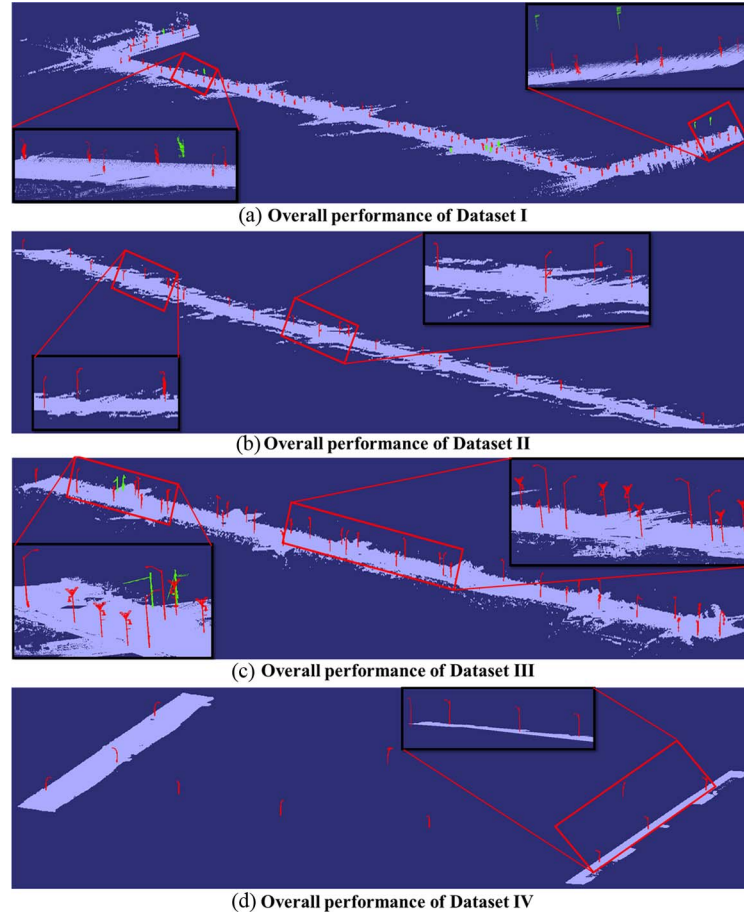


Fig. 14. Overall performance of each data set tested in this paper (the detected street lighting poles, false alarms, and ground are colored in red, green, and gray, respectively). (a) Data set I. (b) Data set II. (c) Data set III. (d) Data set IV.

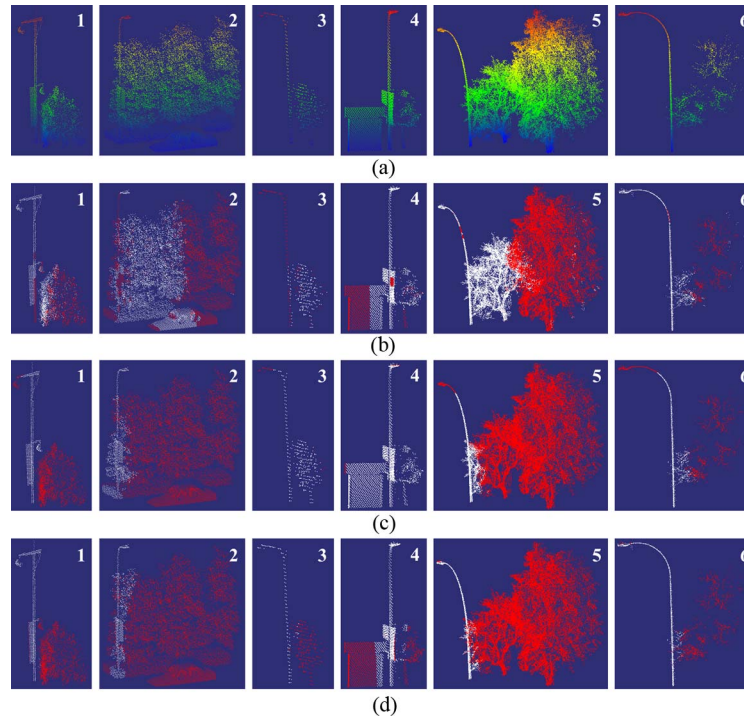


Fig. 15. Comparison of the performance of three graph-cut-based segmentation methods (foreground and background points are colored as white and red, respectively). (a) Raw point cloud of street lighting pole with interferences. (b) Segmentation results of the normalized-cut-based method. (c) Segmentation results of the min-cut-based method. (d) Segmentation results of the proposed method.

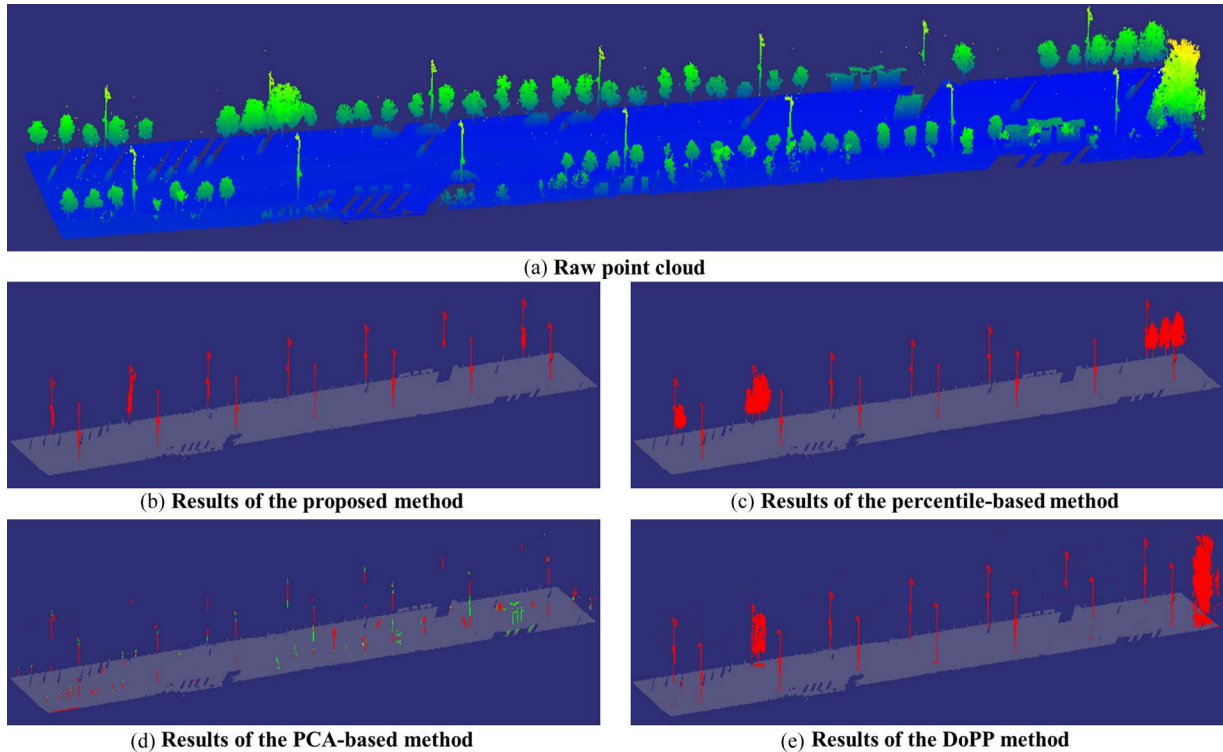


Fig. 16. Comparison of the performances of existing approaches on street lighting pole extraction (or recognition in this paper). (a) Testing point cloud after preprocessing. (b) Performance of the proposed method. (c) Performance of the percentile-based method. (d) Performance of the PCA-based method (points with linear features are colored in red; points that represent the boundary and edges are colored in green). (e) Performance of the DoPP algorithm.

sets with the sample street lighting poles' model database. The proposed method has been tested on four data sets from different sources having different densities containing both the urban and suburb areas. Experimental results indicate that the proposed approach achieved a true positive rate of 90%. Our future work includes an investigation on how the number of a single Gaussian model in the mixture of Gaussian affects modeling performance. A discussion on this relation and its experimental analysis is also under our consideration.

#### ACKNOWLEDGMENT

The authors would like to thank the City of Calgary Council and Optech Corporation for providing the mobile LiDAR data. They would also like to thank Dr. J. Peethambaran for his great help in proofreading.

#### REFERENCES

- [1] A. Teichman, J. Levinson, and S. Thrun, "Towards 3-D object recognition via classification of arbitrary object tracks," in *Proc. IEEE ICRA*, 2011, pp. 4034–4041.
- [2] J. Levinson, M. Montemerlo, and S. Thrun, "Map-based precision vehicle localization in urban environments," in *Proc. Robot., Sci. Syst.*, Atlanta, GA, USA, Jun. 2007, pp. 1–8.
- [3] R. Li, W. Wang, and H.-Z. Tseng, "Detection and location of objects from mobile mapping image sequences by Hopfield neural networks," *Photogramm. Eng. Remote Sens.*, vol. 65, no. 10, pp. 1199–1205, 1999.
- [4] C. V. Tao, "Database-guided automatic inspection of vertically structured transportation objects from mobile mapping image sequences," *Photogramm. Eng. Remote Sens.*, vol. 67, no. 12, pp. 1401–1409, 2001.
- [5] I. Abuhadrous, S. Ammoun, F. Nashashibi, F. Goulette, and C. Lourgeau, "Digitizing and 3D modeling of urban environments and roads using vehicle-borne laser scanner system," in *Proc. IEEE/RSJ Int. Conf. IROS*, 2004, vol. 1, pp. 76–81.
- [6] A. Boyko and T. Funkhouser, "Extracting roads from dense point clouds in large scale urban environment," *ISPRS J. Photogramm. Remote Sens.*, vol. 66, no. 6, pp. S2–S12, 2011.
- [7] W. Zhang, "LiDAR-based road and road-edge detection," in *Proc. IEEE Intell. Veh. Symp.*, San Diego, CA, USA, Jun. 2010, pp. 845–848.
- [8] K. C. Fuerstenberg, K. C. J. Dietmayer, and V. Willhoeft, "Pedestrian recognition in urban traffic using a vehicle based multilayer laserscanner," in *Proc. IEEE Intell. Veh. Symp.*, 2002, vol. 1, pp. 31–35.
- [9] T. L. Rakusz and A. Barsi, "LIDAR-based vehicle segmentation," in *Proc. Int. Conf. Photogramm. Remote Sens.*, Istanbul, Turkey, 2004, pp. 156–159.
- [10] B. J. Li, Q. Q. Li, W. Z. Shi, and F. F. Wu, "Feature extraction and modeling of urban building from vehicle-borne laser scanning data," in *Proc. Int. Archives Photogramm., Remote Sens. Spatial Inf. Sci.*, 2004, pp. 934–940.
- [11] P. Shi and G. Vosselman, "Knowledge based reconstruction of building models from terrestrial laser scanning data," *ISPRS J. Photogramm. Remote Sens.*, vol. 64, no. 6, pp. 575–584, 2009.
- [12] H. Zuowei, X. Chi, and F. Liu, "A methodology for extraction building facades from VLS," in *Proc. 3rd IDCMA*, 2012, pp. 77–80.
- [13] J. Martínez *et al.*, "Automatic processing of terrestrial laser scanning data of building facades," *Autom. Construct.*, vol. 22, pp. 298–305, 2012.
- [14] R. Wang, F. Ferrie, and J. Macfarlane, "A method for detecting windows from mobile LiDAR data," *Photogramm. Eng. Remote Sens.*, vol. 78, no. 11, pp. 1129–1140, 2012.
- [15] C. Brenner, "Extraction of Features from Mobile Laser Scanning Data for Future Driver Assistance Systems," in *Advances in GIScience*, ser. Lecture Notes in Geoinformation and Cartography. New York, NY, USA: Springer-Verlag, 2009, pp. 25–42.
- [16] M. R. Shi Pu, G. George Vosselman, and S. Oude Elberink, "Recognizing basic structures from mobile laser scanning data for road inventory studies," *ISPRS J. Photogramm. Remote Sens.*, vol. 66, no. 6, pp. S28–S39, 2011.
- [17] Y. Yu, J. Li, H. Guan, C. Wang, and J. Yu, "Semiautomated extraction of street light poles from mobile LiDAR point-clouds," *IEEE Trans. Geosci. Remote Sens.*, vol. 53, no. 3, pp. 1374–1386, Mar. 2015.

- [18] A. Nurunnabi *et al.*, "Robust segmentation in laser scanning 3D point cloud data," in *Proc. Int. Conf. Digit. Image Comput. Techn. Appl.*, 2012, pp. 1–8.
- [19] P. J. Besl and R. C. Jain, "Segmentation through variable-order surface fitting," *IEEE Trans. Pattern Anal. Mach. Intell.*, vol. 10, no. 2, pp. 167–192, Mar. 1988.
- [20] T. Rabbani, F. V. D. Heuel, and G. Vosselmann, "Segmentation of point clouds using smoothness constraint," *Int. Archives Photogramm., Remote Sens. Spatial Inf. Sci.*, vol. 36, no. 5, pp. 248–253, 2006.
- [21] M. Lehtomäki *et al.*, "Detection of vertical pole-like objects in a road environment using vehicle-based laser scanning data," *Remote Sens.*, vol. 2, no. 3, pp. 641–664, 2010.
- [22] R. B. Rusu, N. Blodow, Z. C. Marton, and M. Beetz, "Close-range scene segmentation and reconstruction of 3D point cloud maps for mobile manipulation in domestic environments," in *Proc. IEEE/RSJ Int. Conf. Intell. Robot. Syst.*, 2009, pp. 1–6.
- [23] D. S. Ee Hui Lim, "Multi-scale conditional random fields for over-segmented irregular 3D point-clouds classification," in *Proc. Comput. Vis. Pattern Recog. Workshops*, 2008, pp. 1–7.
- [24] D. S. Ee Hui Lim, "3D terrestrial lidar classifications with super-voxels and multi-scale conditional random fields," *Comput.-Aided Des.*, vol. 41, no. 10, pp. 701–710, 2009.
- [25] A. K. Aijazi, P. Checchin, and L. Trassoudaine, "Segmentation based classification of 3D urban point clouds: A super-voxel based approach with evaluation," *Remote Sens.*, vol. 5, no. 4, pp. 1624–1650, 2013.
- [26] Z. D. Bisheng Yang, G. Zhao, and W. Dai, "Hierarchical extraction of urban objects from mobile laser scanning data," *ISPRS J. Photogramm. Remote Sens.*, vol. 99, pp. 45–57, 2015.
- [27] T. F. Aleksey Golovinskiy, "Min-cut based segmentation of point clouds," in *Proc. IEEE 12th ICCV Workshops*, 2009, pp. 39–46.
- [28] H. Yokoyama, H. Date, S. Kanai, and H. Takeda, "Detection and classification of pole-like objects from mobile laser scanning data of urban environments," *Int. J. CAD/CAM*, vol. 13, no. 2, pp. 31–40, 2013.
- [29] J. Shi and J. Malik, "Normalized cuts and image segmentation," *IEEE Trans. Pattern Anal. Mach. Intell.*, vol. 22, no. 8, pp. 888–905, Aug. 2000.
- [30] Y. Boykov, O. Veksler, and R. Zabih, "Fast approximate energy minimization via graph cuts," *IEEE Trans. Pattern Anal. Mach. Intell.*, vol. 23, no. 11, pp. 1222–1239, Nov. 2001.
- [31] Y. Yu, J. Li, H. Guan, F. Jia, and C. Wang, "Three-dimensional object matching in mobile laser scanning point clouds," *IEEE Geosci. Remote Sens. Lett.*, vol. 12, no. 3, pp. 492–496, Mar. 2015.
- [32] R. B. Rusu, "Semantic 3D object maps for everyday manipulation in human living environments," Ph.D. dissertation, Technische Universität München, Munich, Germany, 2009.
- [33] V. K. Carsten Rother and A. Blake, "'GrabCut'—Interactive foreground extraction using iterated graph cuts," *ACM Trans. Graph.*, vol. 23, no. 3, pp. 309–314, 2004.
- [34] R. Adams and L. Bischof, "Seeded region growing," *IEEE Trans. Pattern Anal. Mach. Intell.*, vol. 16, no. 6, pp. 641–647, Jun. 1994.
- [35] L. Vincent and P. Soille, "Watersheds in digital spaces: An efficient algorithm based on immersion simulations," *IEEE Trans. Pattern Anal. Mach. Intell.*, vol. 13, no. 6, pp. 583–598, Jun. 1991.
- [36] J. Canny, "Computational approach to edge detection," *IEEE Trans. Pattern Anal. Mach. Intell.*, vol. 8, no. 6, pp. 679–698, Jun. 1986.
- [37] O. Veksler, "Star shape prior for graph-cut image segmentation," in *Computer Vision—ECCV*. Berlin, Germany: Springer-Verlag, 2008, pp. 454–467.
- [38] M. Körtgen, G. J. Park, M. Novotni, and R. Klein, "3D shape matching with 3D shape contexts," in *Proc. 7th Central Eur. Semin. Comput. Graph.*, Budmerice, Slovakia, 2003, vol. 3, pp. 5–17.
- [39] I. T. Jolliffe, *Principal Component Analysis*, 2nd ed., ser. Springer Series in Statistics. New York, NY, USA: Springer-Verlag, 2002.
- [40] G. Sfikas, C. Constantinopoulos, A. Likas, and N. P. Galatsanos, "An analytic distance metric for Gaussian mixture models with application in image retrieval," in *Proc. ICANN, Formal Models Appl.*, 2005, vol. 3697, pp. 835–840.
- [41] K. Fukunaga, "Introduction to Statistical Pattern Recognition," 2nd ed. San Diego, CA, USA: Academic, 1990.
- [42] D. M. W. Powers, "Evaluation: From precision, recall and F-measure to ROC, informedness, markedness and correlation," *J. Mach. Learn. Technol.*, vol. 2, no. 1, pp. 37–63, 2011.
- [43] D. D. L. Sherif Ibrahim El-Halawany, "Detection of road poles from mobile terrestrial laser scanner point cloud," in *Proc. IEEE Int. Workshop M2RSM*, 2011, pp. 1–6.
- [44] Y. Hu, X. L., J. Xie, and L. Guo, "A novel approach to extracting street lamps from vehicle-borne laser data," in *Proc. IEEE 19th Int. Conf. Geoinf.*, Shanghai, China, 2011, pp. 1–6.
- [45] A. Bhattacharyya, "On a measure of divergence between two multinomial populations," *Indian J. Statist.*, vol. 7, no. 4, pp. 401–406, 1946.



**Han Zheng** received the B.S. and M.S. degrees in geodesy and geomatics engineering from Wuhan University, Wuhan, China, in 2011 and 2013, respectively. He is currently working toward the Master's degree in digital image system in the Department of Geomatics Engineering, University of Calgary, Calgary, AB, Canada.

His current research interests include laser measurement application, computer vision, digital image processing, and object recognition from three-dimensional point clouds.



**Ruisheng Wang** received the B.Eng. degree in photogrammetry and remote sensing from Wuhan University, Wuhan, China, the M.Sc.E. degree in geomatics engineering from the University of New Brunswick, Fredericton, Canada, and the Ph.D. degree in electrical and computer engineering from McGill University, Montréal, Canada.

In 2012, he joined the Department of Geomatics Engineering, University of Calgary, Calgary, Canada, as an Assistant Professor. Prior to that, he was an Industrial Researcher with HERE Maps, Chicago, IL, USA, since 2008. His current research interests include geomatics and computer vision.



**Sheng Xu** received the M.S. degree in computer science and technology from Nanjing Forestry University, Nanjing, China, in 2010. He is currently working toward the Ph.D. degree in the Department of Geomatics Engineering, University of Calgary, Calgary, AB, Canada.

His current research interests include computer vision, mobile LiDAR data processing, and information extraction from 3-D point clouds.